A superconducting magnetic energy storage based current-type interline dynamic voltage restorer for transient power quality enhancement of composited data center and renewable energy source power system

Jian Xun Jin[1], Qian Zhou[1], Ruo Huan Yang[1]*, You Jin Li[1], Hao Li[1], You Guang Guo[2], Jian Guo Zhu[3]

1 School of Electrical Automation and Information Engineering, Tianjin University, Tianjin 300072, China
2 School of Electrical and Data Engineering, University of Technology Sydney, Ultimo, NSW 2007, Australia
3 School of Electrical and Information Engineering, University of Sydney, Camperdown, NSW 2006, Australia
*Corresponding e-mail: yrh9312@163.com

***Abstract*—Simultaneous protection of sensitive renewable power generators and sensitive loads under transient voltage disturbances is an urgent issue in current power systems. Most existing solutions are based on separate custom power devices and energy storage systems. To efficiently utilize renewable energy under voltage sags and reduce energy storage capacity, a current-source-inverter interline dynamic voltage restorer (CSI-IDVR) based on superconducting magnetic energy storage (SMES) is proposed. The current source topology is designed for the IDVR to obtain a more appropriate current rise limitation and a lower number of switches. The CSI-based voltage dual control is designed and implemented to suppress the voltage oscillations, ensuring the transient stability of the sensitive renewable power generator and sensitive loads during asymmetric faults of the grid. An internet data center (IDC) combined with a typical renewable energy generator, i.e., doubly-fed induction generator (DFIG) is analyzed. Under transient voltage disturbances, the proposed CSI-IDVR can maintain the appropriate voltage profiles of the DFIG and IDC. Compared to the separate DVRs, the required SMES capacity in the CSI-IDVR can be substantially reduced. The feasibility and performance of the proposed CSI-IDVR are verified by numerical simulation.**

***Keywords*—Internet data center, superconducting magnetic energy storage, doubly-fed induction generator, current-source-inverter, interline dynamic voltage restorer, power quality.**

0. Nomenclature

$C_{\mathrm{f}}, L_{\mathrm{f}}$	Capacitance and inductance in the CL filter, respectively
$\boldsymbol{F}$	Voltage and current vector
f_α, f_β	Amplitude of the vector component on the α and β axes, respectively
I_{SMES0}	Initial current of SMES
I'_{SMES}	Current of SMES after voltage sag
$I_{\mathrm{SMES,op}}$	Operating current of SMES
$I_{\mathrm{o1}\langle 1\rangle}, I_{\mathrm{o2}\langle 1\rangle}$	Root-mean-square values of the output currents fundamental components of converters on the DFIG and IDC sides, respectively
$I_{\mathrm{g1}}, I_{\mathrm{g2}}$	Transmission currents of DFIG and IDC, respectively
L_{SMES}	Inductance of superconducting coil
L_{m}	Mutual inductance
$P_{\mathrm{DFIG}}, P_{\mathrm{IDC}}$	Output power of DFIG and input power of IDC, respectively
$P^*_{\mathrm{DFIG}}, P^*_{\mathrm{IDC}}$	Rated power of DFIG and IDC, respectively
$\Delta P_{\mathrm{DFIG}}, \Delta P_{\mathrm{IDC}}$	Fluctuated power of DFIG and IDC, respectively
P_{SMES}	Power exchange of the SMES
$P'_{\mathrm{DFIG}}, P'_{\mathrm{IDC}}$	Output power of DFIG terminal and input power of IDC terminal, respectively
p	Voltage sag ratio
t_{sag}	Duration time of voltage sag
τ_{s}	Time constant of the stator
σ	Leakage coefficient
ω_1	Angular frequency of grid
φ_{ou+}, φ_{oi+}	Voltage initial phase and current initial phase of IDC side, respectively
φ_{ou-}, φ_{oi-}	Initial phases of negative sequence voltages and currents of IDC side, respectively
Subscript c	Compensation variables of the DVR
Subscripts $\mathrm{DFIG}, \mathrm{IDC}$	Variables of DFIG side and IDC side, respectively
Subscript dq	Variables in the dq synchronous rotating reference frame
Subscripts d, q	Components of the variable on the *d*-axis and the *q*-axis, respectively
Subscript g	Grid side variables
Subscript o	Output variables of the converter

Subscripts $\mathrm{P,N}$	Positive- and negative- sequence components of voltage or current, respectively
Subscript ref	Reference value of variables
Subscripts $\mathrm{s,r}$	Variables in stator and rotor sides of DFIG, respectively
Subscript $\alpha\beta$	Variables in the stationary $\alpha\beta$ reference frame
Subscripts $"+","-"$	Positive and negative sequence components, respectively
Superscript os	Variables in case of asymmetric fault
Superscript sag	Variables in case of symmetric fault
Superscripts $"+","-"$	The (dq^+) and (dq^-) reference frames, respectively

1. Introduction

With the development of network technology and big data applications, the internet data centers (IDCs) have become widely distributed power electronic loads nowadays, which are devoted to collecting and processing a large amount of computing data [1]. An IDC comprising hundreds of servers for data processing will consume a great amount of power. According to the EPRI report, IDCs will consume 20% of the electricity generated in the United States by 2030 [2]. To address the huge energy consumption of the IDCs, in recent years, integrating renewable energy sources, such as photovoltaics and wind turbines, into the IDC power supply system has attracted great attention, and the research on related composite systems has also been carried out [3-5]. Nowadays, IDCs are typically powered jointly by renewable energy power supplies and the utility grid [3].

For wind power generation, doubly-fed induction generators (DFIGs) are widely adopted in the wind power industry because of their excellent performance. A DFIG allows variable-speed power generation, making better use of wind resources under different wind conditions. Its cost is reduced due to the use of 25-30% rated power converters and the control scheme is matured [6,7].

The increased implementation of IDCs and the growing need for internet-based services require a more stable and reliable power supply system having a premium power supply. Power quality issues, especially the symmetrical and asymmetrical voltage sags, have attracted increasing attention in modern power systems [8]. Frequently-occurring voltage quality problems might lead to device data loss, hardware damage, and system crashes, seriously affecting power consumers and utilities and causing irreparable losses. In a data center system, voltage quality problems can lead to: (i) the transformation of operation mode and reconfiguration of structure in the IDC, and (ii) even operational failure of the IDC power supply system. Equipment and labor loss have cost millions of dollars to solve the power system failure [9,10]. Furthermore, the direct connection of the DFIG stator windings to the grid makes it more vulnerable to power quality problems, such as voltage imbalance, low-voltage faults, and grid distortion [11,12]. When DFIGs and IDCs are combined in a power system, the protection of both should be taken more seriously to avoid the influence of voltage quality problems.

Currently, uninterruptable power supplies (UPSs) [13,14], static synchronous compensators (STATCOMs) [15], unified power quality conditioners (UPQCs) [16-18], and dynamic voltage restorers (DVRs) [19,20], etc., are commonly used to solve power quality problems and protect sensitive loads. As an emerging customized power supply equipment, the DVR is an advanced and economical voltage sag mitigation equipment for the distribution system, effectively protecting sensitive generators/loads by injecting a specific serial voltage [21].

A traditional DVR consists of a voltage source inverter (VSI) and an isolation transformer in series with the transmission line between the utility grid and the sensitive loads/generators. The purpose of the DVR is to maintain the voltage profile of the sensitive loads/generators by injecting a certain compensating AC voltage into the three-phase network [12]. Furthermore, considering the potential risk of the system suffering from a severe voltage sag, an additional energy storage device (ESD) is also required to perform energy conversion with the system. The power and response speed of the ESD should be large and fast enough to meet the actual power demand [22]. Various ESDs have been extensively studied to solve the power quality problems of DFIG, such as battery energy storage (BES) [23,24], supercapacitor energy storage (SCES) [25,26], superconducting magnetic energy storage (SMES) [17], and flywheel energy storage (FES) [27, 28]. Among them, SCES and SMES have higher power density and can respond quickly during transient faults to meet the corresponding requirements, while the response speed of BES and FES is slightly inferior.

When multiple sensitive loads in a power system are powered from different feeders, to reduce the overall capital cost of the DVR devices, the concept of interline DVR (IDVR) can be used as the reference [29, 30]. An IDVR comprises multiple serial inverters and transformers, and all the inverters share a common DC bus. It can maintain the voltage levels of various sensitive loads simultaneously, even if they have different voltage levels. Compared to DVR cluster protection systems with independent energy storage units for loads, sharing a common DC link can reduce the size of energy storage capacity and significantly lower the cost of custom power devices [31-35]. However, when a fault occurs in the utility grid and all the feeders experience a voltage sag, the sum of the

required energy capacity of the energy storage in an IDVR is the same as that of separate DVRs. It is noteworthy that the capital cost of the energy storage occupies a large amount of the implementation of IDVR. From this perspective, the capital cost of the DVR cannot be efficiently reduced by interline structure modification.

Suppose the energy of the DC link can be replenished simultaneously by some means when injecting compensating power to sensitive loads. In this case, the required capacity of the energy storage will be substantially reduced, and the IDVR will be capable of mitigating long-duration voltage sags. It is notable that when the DVR is utilized to enhance the low-voltage ride-through (LVRT) capability of renewable energy sources, the produced energy of the renewable sources will be absorbed into the DVR [17, 19, 36]. In view of this, the renewable-based IDC power system exactly fits the above-mentioned mechanism. Besides, compared to the VSI-based DVR, a current-source-inverter (CSI)-based DVR is an emerging serial custom power device that has been broadly investigated recently [37-40]. Different from the VSI, the CSI is equipped with inductive-type energy storage in series with the DC bus to emulate supplying the inverter with a current source and features a lower number of switches, low switching dv/dt [38,41], and structural simplicity. Due to the existence of the inductor, a CSI-based DVR can efficiently constrain the change rate of a fault current during voltage abruption while enhancing the load voltage to the rated profile. The fault current limiting characteristic of the CSI has been incorporated in some custom power devices, such as superconducting fault current limiter – magnetic energy storage (SFCL-MES) [42,43] and CSI-based STATCOM [44]. It is also noteworthy that sensitive loads always have a very strict voltage tolerant curve (within millisecond level) to be compensated under voltage sags [45,46]. To achieve an extremely fast compensating operation, SMES could be an effective solution. As a magnetic ESD, the superconducting inductor can be charged or discharged immediately. Its charge/discharge response time depends almost exclusively on the activation of power electronic switches. What is even more remarkable is that the current-type energy storage characteristic of the SMES matches the current source requirement of the CSI [37, 47].

Following the thoughts mentioned above, an SMES-based CSI-IDVR is proposed and modeled to simultaneously protect the sensitive generator and sensitive load. Fig. 1 shows schematically the composited data center and renewable energy source power system with an SMES-based CSI-IDVR. The renewable power generator (RPG) and the IDC with the same power level are separately connected to the utility grid via individual transformers. During normal operations, RPG does not directly supply power to IDC, but transmits energy to the utility grid. When a voltage sag occurs in the utility grid, the energy can be transferred from the RPG to the IDC. Depending on the power variation of the RPG and IDC influenced by wind speed and active servers, the SMES only needs to correspondingly compensate for the power difference between the RPG and the IDC, which can greatly reduce the SMES capacity requirement in IDVR. A CSI-applicable voltage dual control is also presented and analyzed in this paper, guaranteeing accurate maintenance of the voltage profiles of the RPG and IDC under asymmetrical fault.

The rest of this paper is organized as follows. Section 2 introduces the renewable energy data center power system integrated with SMES-based CSI-IDVR. Section 3 theoretically analyzes the dynamic response of DFIG and IDC under grid fault in detail. Section 4 describes the modeling of the proposed SMES-based CSI-IDVR and presents its control strategies. Simulation results are presented in Section 5 to demonstrate the feasibility of the proposed scheme. Section 6 draws the conclusion.

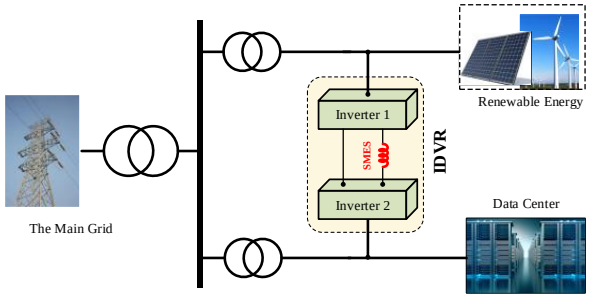

Fig. 1. Scheme of the composited data center and renewable energy source power system with SMES-based CSI-IDVR.

2. Power flow of the renewable energy data center power system with SMES-based CSI-IDVR

Since DFIG is a widely used RPG, this paper takes DFIG as an example to analyze the power flow of the SMES-based CSI-IDVR-integrated system. Fig. 2(a) and (b) show the power flow of the renewable energy data center power system with the SMES based CSI-IDVR under normal and voltage sag fault conditions. It can be seen from the Fig. 2 that the DFIG is connected to the grid via a 690 V/35 kV transformer, the IDC is connected to the grid via a 1 kV /35 kV transformer, and two current-source DVRs are connected in series with the transmission lines in front of the DFIG and IDC, respectively, and share a common DC link and SMES to form the IDVR. The analysis of power flow characteristics under different conditions is summarized as follows:

1) During normal operations, the output power of the DFIG P_{DFIG} varies with the wind speed, and the input power of the IDC P_{IDC} varies with the number of activities of its servers.

The output power of the DFIG and the input power of the IDC can be expressed as follows:

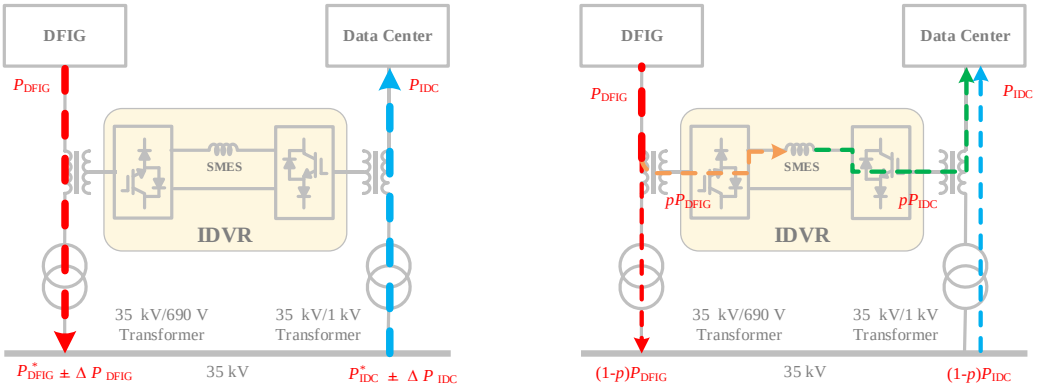

Fig. 2. Power flow of the renewable energy data center power system under different operations, (a) normal operation, (b) voltage sag condition.

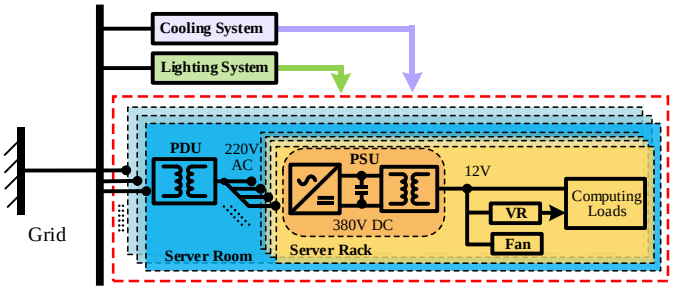

Fig. 3. Scheme of the IDC with AC power system.

$$\begin{cases} P_{\mathrm{DFIG}} = P^*_{\mathrm{DFIG}} + \Delta P_{\mathrm{DFIG}} \\ P_{\mathrm{IDC}} = P^*_{\mathrm{IDC}} + \Delta P_{\mathrm{IDC}} \end{cases} \quad (1)$$

where P^*_{DFIG} and P^*_{IDC} represent the rated power of DFIG and IDC, respectively. The fluctuated power of the DFIG and IDC, i.e., ΔP_{DFIG} and ΔP_{IDC}, are variable.

During voltage sag conditions, IDVR will quickly maintain the voltage levels of DFIG and IDC to improve the LVRT capability of DFIG and ensure the normal operation of IDC. According to (1), there are three different relationships between P_{DFIG} and P_{IDC}:

2) When $P_{\mathrm{DFIG}} > P_{\mathrm{IDC}}$, the SMES will absorb part of the power of the DFIG, and the power exchange of the SMES P_{SMES} can be expressed as:

$$P_{\mathrm{SMES}} = pP_{\mathrm{IDC}} - pP_{\mathrm{DFIG}} \quad (2)$$

where $pP_{\mathrm{IDC}} < pP_{\mathrm{DFIG}}$. p represent the voltage sag ratio. The power of the DFIG output to the grid P'_{DFIG} and the power of the IDC input from the grid P'_{IDC} can be expressed as follows:

$$\begin{cases} P'_{\mathrm{DFIG}} = (1-p)P_{\mathrm{DFIG}} \\ P'_{\mathrm{IDC}} = (1-p)P_{\mathrm{IDC}} \end{cases} \quad (3)$$

Assuming that the duration of voltage sag, the initial current of SMES, and the current of SMES after voltage sag are t_{sag}, I_{SMES0}, and I'_{SMES}, the following equation can be obtained:

$$\frac{1}{2}L_{\mathrm{SMES}}({I'_{\mathrm{SMES}}}^2 - I^2_{\mathrm{SMES0}}) = (pP_{\mathrm{DFIG}} - pP_{\mathrm{IDC}})t_{\mathrm{sag}} \quad (4)$$

3) When $P_{\mathrm{DFIG}} = P_{\mathrm{IDC}}$, there is $pP_{\mathrm{IDC}} = pP_{\mathrm{DFIG}}$. The output power of the SMES to the IDC is the same as the input power from P_{DFIG}.

4) When $P_{\mathrm{DFIG}} < P_{\mathrm{IDC}}$, the SMES will release part of the energy to compensate IDC. Similarly, the following equation can be obtained:

$$\frac{1}{2}L_{\mathrm{SMES}}({I'_{\mathrm{SMES}}}^2 - I^2_{\mathrm{SMES0}}) = -(pP_{\mathrm{DFIG}} - pP_{\mathrm{IDC}})t_{\mathrm{sag}} \quad (5)$$

3. System component

3.1. The power model of IDC in the system

The Scheme of the IDC with an AC power system is shown in Fig. 3. It mainly consists of a cooling system, a lighting system, power distribution units (PDUs), power supply units (PSUs), voltage regulators (VRs), server fans, and computing loads. AC utility power will be converted in multiple steps within the IDC to different voltage levels. The cooling system, lighting system, and PDUs are connected to the 1 kV common bus and then connected to the grid via a 1 kV/35 kV step-up transformer.

The cooling system generally comprises computer room air handlers, water pumps, chiller, cooling tower, and server fans in server racks [1]. The main function of PDU is to down the voltage to an appropriate level. PUD in this system mainly supplies power to server racks via a 1 kV/220 V transformer. The PSU, which is mainly composed of an AC-DC boost converter and a DC-DC power-electronic transformer, needs to convert the AC voltage in the line into the DC level voltage required by various server components. The PSU has the function of power factor correction, which can avoid presenting a reactive component to the distribution system. A 12 V DC power from PSU will supply power to VR, server fan, and computing load in this system.

1) To explain the operation status of the IDC under transient fault in detail, it is necessary to establish a mathematical model. Under normal operation, the complex power obtained by the IDC from the grid in the stationary $\alpha\beta$ reference frame can be expressed as:

$$S^*_{\mathrm{IDC}} = P^*_{\mathrm{IDC}} + jQ^*_{\mathrm{IDC}} = \frac{3}{2}\boldsymbol{U}^*_{\mathrm{IDC}\alpha\beta} \cdot \hat{\boldsymbol{I}}^*_{\mathrm{IDC}\alpha\beta} \quad (6)$$

where P^*_{IDC} and Q^*_{IDC} are the rated active and reactive power of the IDC, respectively, $\boldsymbol{U}^*_{\mathrm{IDC}\alpha\beta}$ and $\boldsymbol{I}^*_{\mathrm{IDC}\alpha\beta}$ are rated terminal voltage and current of the IDC under $\alpha\beta$ model, respectively. $\hat{\boldsymbol{I}}^*_{\mathrm{IDC}\alpha\beta}$ is the conjugate of the current $\boldsymbol{I}^*_{\mathrm{IDC}\alpha\beta}$.

2) Assuming a symmetric voltage sag occurs in the power system with a depth of p at t=0, the IDC terminal voltage $\boldsymbol{U}_{\mathrm{IDC}\alpha\beta}$ and current $\boldsymbol{I}_{\mathrm{IDC}\alpha\beta}$ can be expressed as:

$$\boldsymbol{U}_{\mathrm{IDC}\alpha\beta}(t)=\begin{cases}U_{\mathrm{IDC}}^{*}\mathrm{e}^{j(\omega_1 t+\varphi_{ou+})}, & t<0\\ (1-p)U_{\mathrm{IDC}}^{*}\mathrm{e}^{j(\omega_1 t+\varphi_{ou+})}, & t\geq 0\end{cases} \tag{7}$$

$$\boldsymbol{I}_{\mathrm{IDC}\alpha\beta}(t)=\begin{cases}I_{\mathrm{IDC}}^{*}\mathrm{e}^{j(\omega_1 t+\varphi_{oi+})}, & t<0\\ (1-p)I_{\mathrm{IDC}}^{*}\mathrm{e}^{j(\omega_1 t+\varphi_{oi+})}, & t\geq 0\end{cases} \tag{8}$$

where ω_1, φ_{ou+} and φ_{oi+} represent the angular frequency of the grid and voltage and current initial phase, respectively. The complex power under voltage sag fault can be then derived as:

$$S_{\mathrm{IDC}}^{\mathrm{sag}}=(1-p)^2\frac{3}{2}\boldsymbol{U}_{\mathrm{IDC}\alpha\beta}^{*}\cdot\hat{\boldsymbol{I}}_{\mathrm{IDC}\alpha\beta}^{*}$$
$$=(1-p)^2(P_{\mathrm{IDC}}^{*}+jQ_{\mathrm{IDC}}^{*}) \tag{9}$$

3) When an asymmetrical voltage sag occurs in the system at t=0, the terminal voltage and current of the IDC can be expressed as:

$$\boldsymbol{U}_{\mathrm{IDC}\alpha\beta}(t)=\begin{cases}U_{\mathrm{IDC}}^{*}\mathrm{e}^{j(\omega_1 t+\varphi_{ou+})}, & t<0\\ U_{\mathrm{IDCP}}\mathrm{e}^{j(\omega_1 t+\varphi_{ou+})}+U_{\mathrm{IDCN}}\mathrm{e}^{j(-\omega_1 t+\varphi_{ou-})}, & t\geq 0\end{cases} \tag{10}$$

$$\boldsymbol{I}_{\mathrm{IDC}\alpha\beta}(t)=\begin{cases}I_{\mathrm{IDC}}^{*}\mathrm{e}^{j(\omega_1 t+\varphi_{oi+})}, & t<0\\ I_{\mathrm{IDCP}}\mathrm{e}^{j(\omega_1 t+\varphi_{oi+})}+I_{\mathrm{IDCN}}\mathrm{e}^{j(-\omega_1 t+\varphi_{oi-})}, & t\geq 0\end{cases} \tag{11}$$

where φ_{ou-} and φ_{oi-} represent the initial phases of negative sequence voltages and currents, respectively. Subscripts P, N represent the positive- and negative-sequence components of the amplitudes, respectively. Substituting (10) and (11) into (6), the complex power expression under asymmetric fault can be obtained as:

$$S_{\mathrm{IDC}}^{\mathrm{os}}=\frac{3}{2}\big[(U_{\mathrm{IDCP}}\mathrm{e}^{j(\omega_1 t+\varphi_{ou+})}+U_{\mathrm{IDCN}}\mathrm{e}^{j(-\omega_1 t+\varphi_{ou-})})\cdot(I_{\mathrm{IDCP}}\mathrm{e}^{j(\omega_1 t+\varphi_{oi+})}+I_{\mathrm{IDCN}}\mathrm{e}^{j(-\omega_1 t+\varphi_{oi-})})\big]$$
$$=\frac{3}{2}\big[U_{\mathrm{IDCP}}I_{\mathrm{IDCP}}\mathrm{e}^{j(\varphi_{ou+}-\varphi_{oi+})}+U_{\mathrm{IDCN}}I_{\mathrm{IDCN}}\mathrm{e}^{j(\varphi_{ou-}-\varphi_{oi-})}+$$
$$U_{\mathrm{IDCP}}I_{\mathrm{IDCN}}\mathrm{e}^{j(2\omega_1 t+\varphi_{ou+}-\varphi_{oi-})}+$$
$$U_{\mathrm{IDCN}}I_{\mathrm{IDCP}}\mathrm{e}^{j(-2\omega_1 t+\varphi_{ou-}-\varphi_{oi+})}\big] \tag{12}$$

Analyzing (12), one can simply express the components of the complex power under asymmetrical fault as follows:

$$S_{\mathrm{IDC}}^{\mathrm{os}}=P_{\mathrm{IDC0}}^{\mathrm{os}}+jQ_{\mathrm{IDC0}}^{\mathrm{os}}+$$
$$\underbrace{P_{\mathrm{IDCcos2}}\cos(2\omega_1 t)+P_{\mathrm{IDCsin2}}\sin(2\omega_1 t)}_{P_{IDC2}^{\mathrm{os}}}+$$
$$j[\underbrace{Q_{\mathrm{IDCcos2}}\cos(2\omega_1 t)+Q_{\mathrm{IDCsin2}}\sin(2\omega_1 t)}_{Q_{\mathrm{IDC2}}^{\mathrm{os}}}] \tag{13}$$

The existence of $P_{\mathrm{IDC2}}^{\mathrm{os}}$ and $Q_{\mathrm{IDC2}}^{\mathrm{os}}$ indicate that under unbalanced voltage faults, there are active and reactive power fluctuations with twice the grid frequency in addition to the average active and reactive power transmitted from the grid. It will significantly affect the operation of the IDC. The DC bus voltage of the server rack will contain a DC oscillation component with the frequency of $2\omega_1$, and the computing loads will be influenced. The motors of the cooling system may be destroyed, causing a tremendous loss of revenue.

3.2. Modeling of DFIG under voltage sags

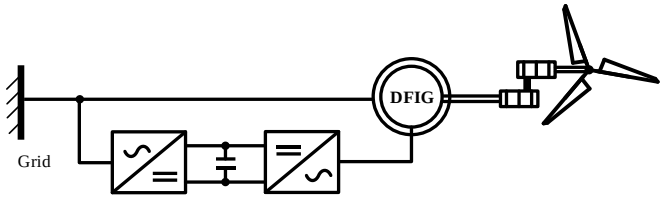

Fig. 4. Scheme of the DFIG with AC power system.

The scheme of the DFIG with an AC power system is shown in Fig. 4. The stator of the DFIG is connected to the grid via a 690 V/35 kV transformer, and the rotor of the DFIG is connected to a back-to-back PWM converter.

To illustrate the transient dynamics of the DFIG in the case of symmetrical and asymmetrical voltage sags, a theoretical analysis is carried out to describe the responses of the critical variables in DFIG.

The DFIG stator and rotor voltages and flux linkages in the stationary $\alpha\beta$ reference frame can be expressed as [48]:

$$\begin{cases}\boldsymbol{U}_{s\alpha\beta}=R_{\mathrm{s}}\boldsymbol{I}_{s\alpha\beta}+\frac{\mathrm{d}\boldsymbol{\psi}_{s\alpha\beta}}{\mathrm{d}t}\\ \boldsymbol{U}_{r\alpha\beta}=R_{\mathrm{r}}\boldsymbol{I}_{r\alpha\beta}+\frac{\mathrm{d}\boldsymbol{\psi}_{r\alpha\beta}}{\mathrm{d}t}-j\omega_{\mathrm{r}}\boldsymbol{\psi}_{r\alpha\beta}\\ \boldsymbol{\psi}_{s\alpha\beta}=L_{\mathrm{s}}\boldsymbol{I}_{s\alpha\beta}+L_{\mathrm{m}}\boldsymbol{I}_{s\alpha\beta}\\ \boldsymbol{\psi}_{r\alpha\beta}=L_{\mathrm{m}}\boldsymbol{I}_{s\alpha\beta}+L_{\mathrm{r}}\boldsymbol{I}_{r\alpha\beta}\end{cases} \tag{14}$$

where $\boldsymbol{U}$, $\boldsymbol{I}$ and $\boldsymbol{\psi}$ represent the vector form of voltage, current and flux linkage, respectively. R, L and ω represent the resistance, inductance, and angular frequency, respectively. Subscripts s and r represent the stator side and rotor side, respectively. L_{m} is the mutual inductance.

By synthesizing four equations in (14), the space vector of the rotor voltage can be obtained as [36]:

$$\boldsymbol{U}_{r\alpha\beta}=(R_{\mathrm{r}}-j\omega_{\mathrm{r}}\sigma L_{\mathrm{r}})\boldsymbol{I}_{r\alpha\beta}+\sigma L_{\mathrm{r}}\frac{\mathrm{d}}{\mathrm{d}t}\boldsymbol{I}_{r\alpha\beta}$$
$$+\frac{L_{\mathrm{m}}}{L_{\mathrm{s}}}(\boldsymbol{U}_{s\alpha\beta}-R_{\mathrm{s}}\boldsymbol{I}_{s\alpha\beta}-j\omega_{\mathrm{r}}\boldsymbol{\psi}_{s\alpha\beta}) \tag{15}$$

where $\sigma=1-L_{\mathrm{m}}^2/L_{\mathrm{s}}L_{\mathrm{r}}$ is the leakage coefficient. The stator voltage in the stationary $\alpha\beta$ reference frame is a rotation vector rotating at the synchronous speed ω_{s}, whose stator voltage amplitude is U_{s}. It can be expressed as:

$$\boldsymbol{U}_{s\alpha\beta}=U_{\mathrm{s}}\mathrm{e}^{j\omega_{\mathrm{s}}t} \tag{16}$$

Neglecting the stator resistance R_{s} and substituting (16) into the (14), the expression of flux linkage can be obtained as follows:

$$\boldsymbol{\psi}_{s\alpha\beta}=\int\boldsymbol{U}_{s\alpha\beta}=\frac{U_{\mathrm{s}}\mathrm{e}^{j\omega_{\mathrm{s}}t}}{j\omega_{\mathrm{s}}} \tag{17}$$

According to (17), (15) can be rewritten as:

$$\boldsymbol{U}_{r\alpha\beta}=\underbrace{(R_{\mathrm{r}}-j\omega_{\mathrm{r}}\sigma L_{\mathrm{r}})\boldsymbol{I}_{r\alpha\beta}+\sigma L_{\mathrm{r}}\frac{\mathrm{d}}{\mathrm{d}t}\boldsymbol{I}_{r\alpha\beta}}_{\boldsymbol{U}_{r\alpha\beta RL}}+\underbrace{\frac{L_{\mathrm{m}}}{L_{\mathrm{s}}}(sU_{\mathrm{s}}\mathrm{e}^{j\omega_{\mathrm{s}}t})}_{\boldsymbol{E}_{r\alpha\beta}} \tag{18}$$

where $\boldsymbol{U}_{r\alpha\beta RL}$ is the voltage drop generated by the rotor current flowing through the rotor resistance R_{r} and transient inductive reactance σL_{r}, $\boldsymbol{E}_{r\alpha\beta}$ is the induced electromotive force generated by the rotor flux linkage, and $s=(\omega_{\mathrm{s}}-\omega_{\mathrm{r}})/\omega_{\mathrm{s}}$ is the slip.

Assuming a symmetrical voltage sag fault with a depth of p occurs in the system at *t*=0, the (16) can be rewritten as:

$$\boldsymbol{U}_{s\alpha\beta}(t)=\begin{cases}U_{\mathrm{s}}\mathrm{e}^{j\omega_{\mathrm{s}}t}, & t<0\\(1-p)U_{\mathrm{s}}\mathrm{e}^{j\omega_{\mathrm{s}}t}, & t\geq 0\end{cases} \tag{19}$$

From (17) and (19), it is apparent that the stator flux linkage at a steady state can be expressed as:

$$\boldsymbol{\psi}_{s\alpha\beta}(t)=\begin{cases}\frac{U_{\mathrm{s}}\mathrm{e}^{j\omega_{\mathrm{s}}t}}{j\omega_{\mathrm{s}}}, & t<0\\\frac{(1-p)U_{\mathrm{s}}\mathrm{e}^{j\omega_{\mathrm{s}}t}}{j\omega_{\mathrm{s}}}, & t\geq 0\end{cases} \tag{20}$$

Assuming that the rotor side of DFIG is open-circuited, i.e., $\boldsymbol{I}_{s\alpha\beta}=0$, following the (14), the stator voltage can be obtained as follows:

$$\boldsymbol{U}_{s\alpha\beta}=\frac{R_{\mathrm{s}}}{L_{\mathrm{s}}}\boldsymbol{\psi}_{s\alpha\beta}+\frac{\mathrm{d}}{\mathrm{d}t}\boldsymbol{\psi}_{s\alpha\beta} \tag{21}$$

Solving (21) with (20), the stator flux can be further derived as follows:

$$\boldsymbol{\psi}_{s\alpha\beta}(t)=\begin{cases}\frac{1}{j\omega_{\mathrm{s}}}U_{\mathrm{s}}\mathrm{e}^{j\omega_{\mathrm{s}}t}, & t<0\\\frac{1}{j\omega_{\mathrm{s}}}(1-p)U_{\mathrm{s}}\mathrm{e}^{j\omega_{\mathrm{s}}t}+\frac{1}{j\omega_{\mathrm{s}}}pU_{\mathrm{s}}\mathrm{e}^{-t/\tau_{\mathrm{s}}}, & t\geq 0\end{cases} \tag{22}$$

where $\tau_{\mathrm{s}}=L_{\mathrm{s}}/R_{\mathrm{s}}$ is the time constant of the DFIG stator. Substitute (22) into $\boldsymbol{E}_{r\alpha\beta}$ in (18), and convert it to the rotor rotation frame, $\boldsymbol{E}_{\mathrm{r}\alpha\beta}$ can be expressed as:

$$\boldsymbol{E}^{\mathrm{r}}_{\mathrm{r}\alpha\beta}=\frac{L_{\mathrm{m}}}{L_{\mathrm{s}}}[s(1-p)U_{\mathrm{s}}\mathrm{e}^{j(\omega_{\mathrm{s}}-\omega_{\mathrm{r}})t}-(1-s)pU_{\mathrm{s}}\mathrm{e}^{j\omega_{\mathrm{r}}t}\mathrm{e}^{-t/\tau_{\mathrm{s}}}] \tag{23}$$

From (23), $\boldsymbol{E}^{\mathrm{r}}_{\mathrm{r}\alpha\beta}$ contains two components: 1) an AC component rotating counterclockwise at the angular frequency $\omega_{\mathrm{s}}-\omega_{\mathrm{r}}$, whose amplitude is directly proportional to s and $(1-p)U_{\mathrm{s}}$; 2) an AC component rotating clockwise at the angular frequency ω_{r} whose amplitude is directly proportional to $(1-s)$ and pU_{s}, decaying with the stator time constant τ_{s}. The amplitude of the second component is substantially large under transient condition, owing to the large values of $(1-s)$ and pU_{s}.

Ignoring the rotor current, from the (14), the expression of the stator current can be obtained as [49]:

$$\boldsymbol{I}_{s\alpha\beta}=\frac{1}{j\omega_{\mathrm{s}}L_{\mathrm{s}}}(1-p)U_{\mathrm{s}}\mathrm{e}^{j\omega_{\mathrm{s}}t}+\frac{1}{j\omega_{\mathrm{s}}L_{\mathrm{s}}}pU_{\mathrm{s}}\mathrm{e}^{-t/\tau_{\mathrm{s}}} \tag{24}$$

From (24), there is mainly an AC component and a decaying DC component in the stator current. Convert the stator current from stationary $\alpha\beta$ reference frame to dq synchronous rotating reference frame, the (24) can be re-expressed as:

$$\boldsymbol{I}_{sdq}=\boldsymbol{I}_{sdq0}+\boldsymbol{I}_{sdq1}\mathrm{e}^{-j\omega_{\mathrm{s}}t}\mathrm{e}^{-t/\tau_{\mathrm{s}}} \tag{25}$$

The output complex power of the stator can be expressed as:

$$\begin{aligned}S^{\mathrm{sag}}_{\mathrm{s}}=P_{\mathrm{s}}+jQ_{\mathrm{s}}&=-\frac{3}{2}\boldsymbol{U}_{sdq}\cdot\hat{\boldsymbol{I}}_{sdq}\\&=-\frac{3}{2}\big(u_{sd}+ju_{sq}\big)\big(i_{sd0}-ji_{sq0}+i_{sd1}\mathrm{e}^{j\omega_{\mathrm{s}}t}\mathrm{e}^{-t/\tau_{\mathrm{s}}}\\&\qquad-ji_{sq1}\mathrm{e}^{j\omega_{\mathrm{s}}t}\mathrm{e}^{-t/\tau_{\mathrm{s}}}\big)\\&=-\frac{3}{2}[u_{sd}i_{sd0}+u_{sq}i_{sq0}+j(u_{sq}i_{sd0}-u_{sd}i_{sq0})\\&\qquad+\big(u_{sd}i_{sd1}+u_{sq}i_{sq1}\big)\mathrm{e}^{j\omega_{\mathrm{s}}t}\mathrm{e}^{-t/\tau_{\mathrm{s}}}\\&\qquad+j\big(u_{sq}i_{sd1}-u_{sd}i_{sq1}\big)\mathrm{e}^{j\omega_{\mathrm{s}}t}\mathrm{e}^{-t/\tau_{\mathrm{s}}}]\end{aligned} \tag{26}$$

Analyzing the components in (26), one can simplify (26) as the following:

$$S^{\mathrm{sag}}_{\mathrm{s}}=P^{\mathrm{sag}}_{\mathrm{s0}}+\mathrm{j}Q^{\mathrm{sag}}_{\mathrm{s0}}+\underbrace{P_{\mathrm{ssin1}}\sin(\omega_{\mathrm{s}}t)\,\mathrm{e}^{-t/\tau_{\mathrm{s}}}}_{P^{\mathrm{sag}}_{\mathrm{s1}}}+ j\underbrace{Q_{\mathrm{ssin1}}\sin(\omega_{\mathrm{s}}t)\,\mathrm{e}^{-t/\tau_{\mathrm{s}}}}_{Q^{\mathrm{sag}}_{\mathrm{s1}}} \tag{27}$$

From (27), when a symmetrical voltage sag fault occurs, besides average active power and reactive power, the stator output power of the DFIG also includes decaying active and reactive power fluctuations with the angular frequency of ω_{s}.

Considering an asymmetrical voltage sag fault in the system at *t*=0, the (19) can be rewritten as:

$$\boldsymbol{U}_{s\alpha\beta}(t)=\begin{cases}U_{\mathrm{s}}\mathrm{e}^{j\omega_{\mathrm{s}}t}, & t<0\\U_{\mathrm{sP}}\mathrm{e}^{j\omega_{\mathrm{s}}t}+U_{\mathrm{sN}}\mathrm{e}^{-j\omega_{\mathrm{s}}t}, & t\geq 0\end{cases} \tag{28}$$

where U_{sP} and U_{sN} are the magnitudes of the positive and negative sequence components of the stator voltage after the voltage sags, respectively. Similar to the solution process of the formula (22), the expression of stator flux linkage can be obtained as:

$$\boldsymbol{\psi}_{s\alpha\beta}(t)=\begin{cases}\frac{1}{j\omega_{\mathrm{s}}}U_{\mathrm{s}}\mathrm{e}^{j\omega_{\mathrm{s}}t} & t<0\\\frac{U_{\mathrm{sP}}\mathrm{e}^{j\omega_{\mathrm{s}}t}}{j\omega_{\mathrm{s}}}+\frac{U_{\mathrm{s}}-U_{\mathrm{sP}}}{j\omega_{\mathrm{s}}}\mathrm{e}^{-t/\tau_{s}}+\frac{U_{\mathrm{sN}}\mathrm{e}^{-j\omega_{\mathrm{s}}t}}{-j\omega_{\mathrm{s}}}+\frac{0-U_{\mathrm{sN}}}{-j\omega_{\mathrm{s}}}\mathrm{e}^{-t/\tau_{\mathrm{s}}} & t\geq 0\end{cases} \tag{29}$$

Substituting formula (29) into the (17), the $\boldsymbol{E}_{r\alpha\beta}$ under asymmetrical fault can be re-expressed as:

$$\begin{aligned}\boldsymbol{E}^{\mathrm{r}}_{\mathrm{r}\alpha\beta}=\frac{L_{\mathrm{m}}}{L_{\mathrm{s}}}[&sU_{\mathrm{sP}}\mathrm{e}^{j(\omega_{\mathrm{s}}-\omega_{\mathrm{r}})t}+(2-s)U_{\mathrm{sN}}\mathrm{e}^{j(-\omega_{\mathrm{s}}-\omega_{\mathrm{r}})t}\\&-(1-s)(U_{\mathrm{s}}-U_{\mathrm{sP}}+U_{\mathrm{sN}})\mathrm{e}^{-j\omega_{\mathrm{r}}t}\mathrm{e}^{-t/\tau_{\mathrm{s}}}\end{aligned} \tag{30}$$

The above expression shows that under an asymmetrical fault, an additional third component of the $\boldsymbol{E}^{\mathrm{r}}_{\mathrm{r}\alpha\beta}$ appears with the angular frequency of $-\omega_{\mathrm{s}}-\omega_{\mathrm{r}}$. Its amplitude is proportional to $(2-s)U_{\mathrm{sN}}$.

Assuming the DFIG rotor is open circuit and ignoring the rotor side current, the stator current, in this case, can be expressed as:

$$\begin{aligned}\boldsymbol{I}_{s\alpha\beta}=&\frac{U_{\mathrm{sP}}\mathrm{e}^{j\omega_{\mathrm{s}}t}}{j\omega_{\mathrm{s}}L_{s}}+\frac{U_{\mathrm{s}}-U_{\mathrm{sP}}}{j\omega_{\mathrm{s}}L_{\mathrm{s}}}\mathrm{e}^{-t/\tau_{\mathrm{s}}}\\&+\frac{U_{\mathrm{sN}}\mathrm{e}^{-j\omega_{\mathrm{s}}t}}{-j\omega_{\mathrm{s}}L_{s}}+\frac{0-U_{\mathrm{sN}}}{-j\omega_{\mathrm{s}}L_{\mathrm{s}}}\mathrm{e}^{-t/\tau_{\mathrm{s}}}\end{aligned} \tag{31}$$

As with the processing of the formula (27), (31) can be rewritten as:

$$\boldsymbol{I}_{sdq}=\boldsymbol{I}_{sdq0}+\boldsymbol{I}_{sdq1}\mathrm{e}^{-j\omega_{\mathrm{s}}t}\mathrm{e}^{-t/\tau_{\mathrm{s}}}+\boldsymbol{I}_{sdq2}\mathrm{e}^{-j2\omega_{\mathrm{s}}t} \tag{32}$$

Under an asymmetrical fault, the stator voltage can be expressed as:

$$\boldsymbol{U}_{sdq}=\boldsymbol{U}_{sdq0}+\boldsymbol{U}_{sdq2}\mathrm{e}^{-j2\omega_{\mathrm{s}}t} \tag{33}$$

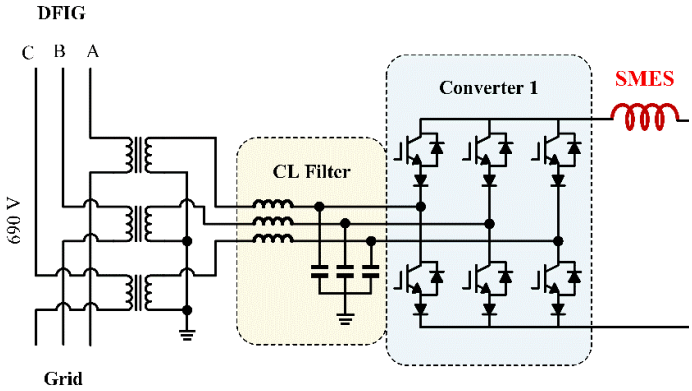

Fig. 5. Schematic diagram of the SMES-based CSI-IDVR.

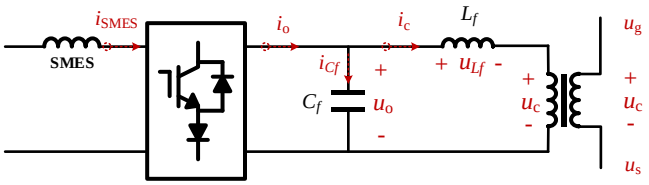

Fig. 6. The equivalent circuit diagram of the converter 1 side grid-connected model.

The output complex power of the stator can be expressed as:

$$S_s^{os} = \frac{3}{2}\boldsymbol{U}_{sdq}\cdot\hat{\boldsymbol{I}}_{sdq} = \frac{3}{2}(\boldsymbol{U}_{sdq0}+\boldsymbol{U}_{sdq2}e^{-j2\omega_s t})(\boldsymbol{I}_{sdq0}+\boldsymbol{I}_{sdq1}e^{j\omega_s t}e^{-t/\tau_s}+\boldsymbol{I}_{sdq2}e^{j2\omega_s t}) \quad (34)$$

Similar to the formula (27), the above formula can be re-expressed as:

$$\begin{aligned} S_s^{os} &= P_{s0}^{os}+jQ_{s0}^{os} \\ &+\underbrace{P_{ssin1}\sin(\omega_s t)e^{-t/\tau_s}+P_{scos1}\cos(\omega_s t)\,e^{-t/\tau_s}}_{P_{s1}^{os}} \\ &+\underbrace{P_{ssin2}\sin(2\omega_s t)+P_{scos2}\cos(2\omega_s t)}_{P_{s2}^{os}} \\ &+j[\underbrace{Q_{ssin1}\sin(\omega_s t)e^{-t/\tau_s}+Q_{scos1}\cos(\omega_s t)\,e^{-t/\tau_s}}_{Q_{s1}^{os}}] \\ &+j[\underbrace{Q_{ssin2}\sin(2\omega_s t)+Q_{scos2}\cos(2\omega_s t)}_{Q_{s2}^{os}}] \end{aligned} \quad (35)$$

Equation (35) shows that during an asymmetrical voltage sag fault the stator output power of DFIG also has active and reactive power fluctuations with angular frequencies of ω_s and $2\omega_s$. The terms P_{s1}^{os} and Q_{s1}^{os} are constantly attenuated with the time constant. These power fluctuations will affect the stability of the whole power generation system and the safety of the hardware.

4. Principle of the SMES-based CSI-IDVR

To regulate the terminal voltages of the IDC and DFIG and balance the power flow under transient voltage disturbances, a SMES-based CSI-IDVR is proposed and modeled. The schematic diagram of the SMES-based CSI-IDVR is presented in Fig. 5. As shown in the Fig. 5, the proposed SMES-based CSI-IDVR structure is symmetrical. Since the module of the CSI is supposed to withstand reverse voltage, each converter is made up of six power electronic devices with reverse-conducting IGBT and a diode. The converter is connected to the lines on both sides in series through three-phase CL filters and transformers, and the SMES is connected in series between the two converters.

4.1. The control of CSI-IDVR

According to the structural symmetry of CSI-IDVR, the grid-connected model of the converter-1 side connected to DFIG is selected for modeling analysis. The equivalent circuit diagram is shown in Fig. 6. In the Fig. 6, u_g is the grid side voltage; u_s is the stator voltage of the DFIG, that is, the DFIG side voltage; C_f and L_f are the capacitance and inductance in the CL filter, respectively; The subscripts c and o represent the compensation variable of the DVR and the output variable of the converter, respectively, and i_{SMES} is the operating current of the SMES.

The basic equation for the Fig. 6 can be obtained as follows [50]:

$$\begin{cases} u_s = u_g - u_c \\ i_o = i_{Cf} + i_c \\ u_o = u_{Lf} + u_c \\ i_{Cf} = C_f\dfrac{du_o}{dt} \\ u_{Lf} = L_f\dfrac{di_c}{dt} \end{cases} \quad (36)$$

Since the value of L_f in the CL filter is generally small, L_f can be ignored for the convenience of calculation, so the reference value u_{oref} of u_o can be calculated by the following formula:

$$u_{oref} \approx u_{cref} = u_{sref} - u_s \quad (37)$$

To precisely control the terminal voltages of the DFIG and IDC, it is necessary to introduce a CSI-appliable dual voltage control. The basic principle of the dual control is introduced as follows.

In the stationary $\alpha\beta$ reference frame, the form of space vector $\boldsymbol{F}$ defining electromagnetic quantity is as follows:

$$\boldsymbol{F}_{\alpha\beta} = f_\alpha + jf_\beta = (f_{\alpha+}+f_{\alpha-})+j(f_{\beta+}+f_{\beta-}) \quad (38)$$

where $\boldsymbol{F}$ is generalized as voltage and current vector. f_α and f_β represent the amplitude of the vector on the α and β axes, respectively. Subscripts "+" and "-"

represent the positive- and negative- sequence components, respectively.

According to Euler's formula $e^{j\gamma}=\cos\gamma+j\sin\gamma$, the following formula can be derived from formula (38):

$$\begin{aligned}\boldsymbol{F}_{\alpha\beta}&=\boldsymbol{F}_{\alpha\beta+}+\boldsymbol{F}_{\alpha\beta-}=\left(f_{\alpha+}+jf_{\beta+}\right)+\left(f_{\alpha-}+jf_{\beta-}\right)\\&=\underbrace{f_{\alpha\beta+}e^{j\omega t}}_{\boldsymbol{F}_{\alpha\beta+}}+\underbrace{f_{\alpha\beta-}e^{-j\omega t}}_{\boldsymbol{F}_{\alpha\beta-}}\end{aligned}\tag{39}$$

where $\boldsymbol{F}_{\alpha\beta+}$ and $\boldsymbol{F}_{\alpha\beta-}$ represent the positive- and negative-sequence space vector of $\boldsymbol{F}_{\alpha\beta}$, respectively. For the convenience of analysis, it is defined here that the (dq^+) reference frame rotates counterclockwise at the angular speed of ω, and the (dq^-) reference frame rotates clockwise at the angular speed of $-\omega$. According to (39), the following formula can be obtained:

$$\begin{aligned}\boldsymbol{F}_{dq}^{+}&=\boldsymbol{F}_{\alpha\beta}e^{-j\omega t}=\boldsymbol{F}_{\alpha\beta+}e^{-j\omega t}+\boldsymbol{F}_{\alpha\beta-}e^{-j\omega t}\\&=\boldsymbol{F}_{dq+}^{+}+\boldsymbol{F}_{dq-}^{-}e^{-j2\omega t}\end{aligned}\tag{40}$$

$$\begin{aligned}\boldsymbol{F}_{dq}^{-}&=\boldsymbol{F}_{\alpha\beta}e^{j\omega t}=\boldsymbol{F}_{\alpha\beta+}e^{j\omega t}+\boldsymbol{F}_{\alpha\beta-}e^{j\omega t}\\&=\boldsymbol{F}_{dq-}^{-}+\boldsymbol{F}_{dq+}^{+}e^{j2\omega t}\end{aligned}\tag{41}$$

where superscripts "+" and "-" refer to the (dq^+) and (dq^-) reference frames, respectively. For voltage and current signals, the methods for obtaining $\boldsymbol{F}_{dq+}^{+}$ and $\boldsymbol{F}_{dq-}^{-}$ are shown in Fig. 7.

According to the above analysis, there are four voltage components available to be controlled by Converter 1, namely u_{od+}^{+}, u_{oq+}^{+}, u_{od-}^{-}, u_{oq-}^{-}. Referring to (37), the compensation voltage signals can be expressed as:

$$\begin{cases}u_{odref+}^{+}=u_{sdref+}^{+}-u_{sd+}^{+}\\u_{oqref+}^{+}=u_{sqref+}^{+}-u_{sq+}^{+}\\u_{odref-}^{-}=u_{sdref-}^{-}-u_{sd-}^{-}\\u_{oqref-}^{-}=u_{sqref-}^{-}-u_{sq-}^{-}\end{cases}\tag{42}$$

According to (36), the mathematical model of the CL filter can be obtained as:

$$\begin{cases}i_{od+}^{+}=C_f\dfrac{du_{od+}^{+}}{dt}-\omega_g C_f u_{oq+}^{+}+i_{cd+}^{+}\\i_{oq+}^{+}=C_f\dfrac{du_{oq+}^{+}}{dt}+\omega_g C_f u_{od+}^{+}+i_{cq+}^{+}\\i_{od-}^{-}=C_f\dfrac{du_{od-}^{-}}{dt}-\omega_g C_f u_{oq-}^{-}+i_{cd-}^{-}\\i_{oq-}^{-}=C_f\dfrac{du_{oq-}^{-}}{dt}+\omega_g C_f u_{od-}^{-}+i_{cq-}^{-}\end{cases}\tag{43}$$

where ω_g is the angular frequency of the grid side voltage. $-\omega_g C_f u_{oq+}^{+}$, $\omega_g C_f u_{od+}^{+}$, $-\omega_g C_f u_{oq-}^{-}$ and $\omega_g C_f u_{od-}^{-}$ are the current compensation terms of the CL filter in the corresponding control loop, respectively.

Combining (42) and (43), after introducing the proportional-integral (PI) regulator, the controller can be designed as follows:

$$\begin{cases}i_{odref+}^{+}=\left(k_{pd+}^{+}+\dfrac{k_{id+}^{+}}{s}\right)\left(u_{odref+}^{+}-u_{od+}^{+}\right)-\omega_g C_f u_{oq+}^{+}+i_{cd+}^{+}\\i_{oqref+}^{+}=\left(k_{pq+}^{+}+\dfrac{k_{iq+}^{+}}{s}\right)\left(u_{oqref+}^{+}-u_{oq+}^{+}\right)+\omega_g C_f u_{od+}^{+}+i_{cq+}^{+}\\i_{odref-}^{-}=\left(k_{pd-}^{-}+\dfrac{k_{id-}^{-}}{s}\right)\left(u_{odref-}^{-}-u_{od-}^{-}\right)-\omega_g C_f u_{oq-}^{-}+i_{cd-}^{-}\\i_{oqref-}^{-}=\left(k_{pq-}^{-}+\dfrac{k_{iq-}^{-}}{s}\right)\left(u_{oqref-}^{-}-u_{oq-}^{-}\right)+\omega_g C_f u_{od-}^{-}+i_{cq-}^{-}\end{cases}\tag{44}$$

According to the above analysis, the control diagram of CSI-IDVR is shown in Fig. 8.

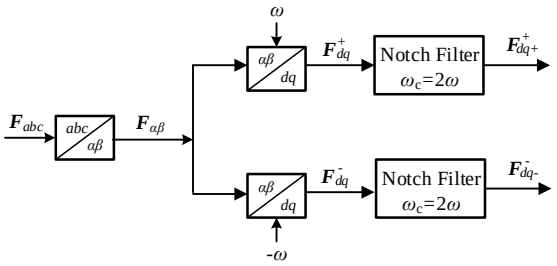

Fig. 7. The sequence decomposition methods for voltage/current signals.

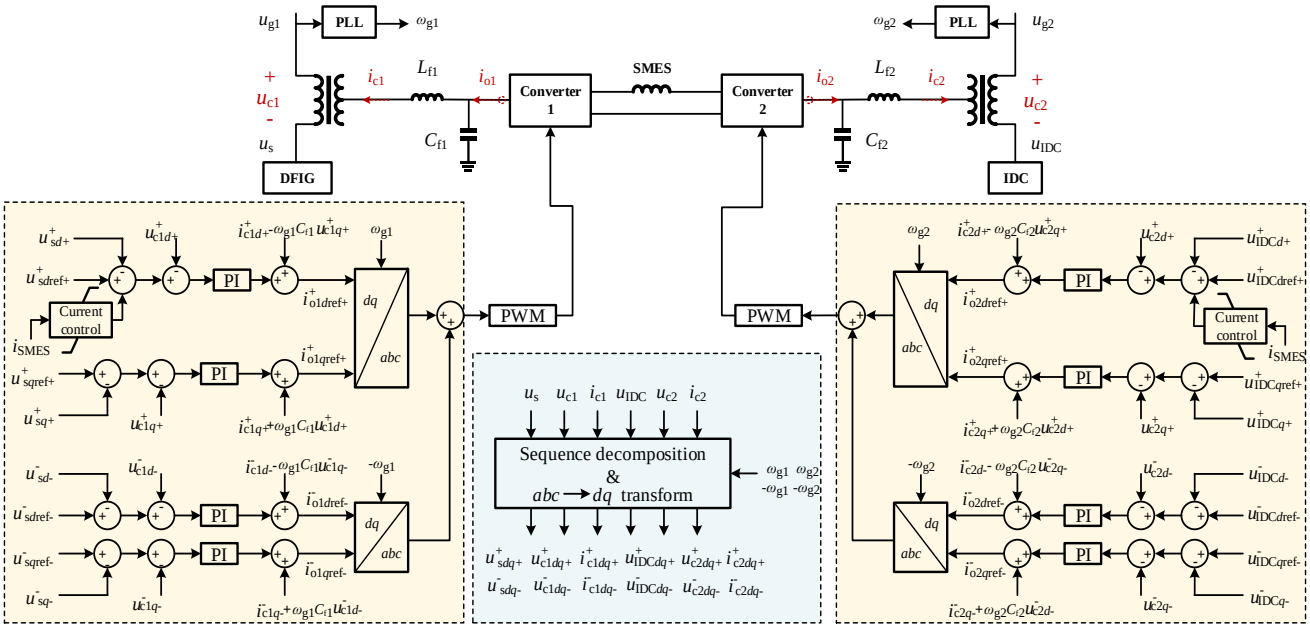

Fig. 8. Entire control scheme of the SMES-based CSI-IDVR.

4.2. Capacity design of the SMES

In this study, two DVRs are connected through a common SMES coil to protect two sensitive loads of DFIG and IDC simultaneously and can realize the energy conversion from DFIG to IDC in case of fault. Compared with two independent DVR protection schemes with two SMES, the required SMES capacity can be greatly reduced, significantly reducing the cost. In addition, using the current source IDVR topology, there is no need to add additional DC/DC converters, which can respond quickly, reduce the number of switches in the device and further reduce the cost.

According to the current relationship of CSI [51], the relationship between the fundamental effective value of CSI output current and the operating current of SMES shall meet the following requirements:

$$I_{\mathrm{SMES,op}} \geq \frac{\pi}{\sqrt{6}} I_{o1\langle 1\rangle} \tag{45}$$

$$I_{\mathrm{SMES,op}} \geq \frac{\pi}{\sqrt{6}} I_{o2\langle 1\rangle} \tag{46}$$

where $I_{o1\langle 1\rangle}$ and $I_{o2\langle 1\rangle}$ are the root-mean-square value of the CSI output fundamental currents. To simplify the analysis, the output currents of the Converter 1 and 2 filtered by CL branches can be regarded as equal to the transmission current I_{g1} and I_{g2}, respectively. Considering the active servers of the IDC and the wind speed variation of the DFIG, the output currents of the DFIG and the input current of the IDC fluctuate in ranges of $I_{\mathrm{g1}} \in [I^*_{\mathrm{g1min}}, I^*_{\mathrm{g1max}}]$ and $I_{\mathrm{g2}} \in [I^*_{\mathrm{g2min}}, I^*_{\mathrm{g2max}}]$, respectively. Therefore, the minimum operating current of SMES $I_{\mathrm{SMES,opmin}}$ can be estimated by:

$$I_{\mathrm{SMES,opmin}} \geq \frac{\pi}{\sqrt{6}} \max\{I_{\mathrm{g1}}, I_{\mathrm{g2}}\} \tag{47}$$

The energy stored in the SMES available for voltage sag compensation is:

$$E^*_{\mathrm{SMES}} = \frac{1}{2} L_{\mathrm{SMES}} I^2_{\mathrm{SMES}} - \frac{1}{2} L_{\mathrm{SMES}} I^2_{\mathrm{SMES,opmin}} \tag{48}$$

As analyzed in Section 2, when $P_{\mathrm{DFIG}} < P_{\mathrm{IDC}}$, the SMES should output specific energy to compensate the IDC. To ensure enough capacity of the SMES to deal with the voltage sag, the operating current of the SMES should simultaneously satisfy the following equation:

$$E^*_{\mathrm{SMES}} \geq (pP^*_{\mathrm{IDCmax}} - pP^*_{\mathrm{DFIGmin}}) t_{\mathrm{sag}} \tag{49}$$

where P^*_{IDCmax} and P^*_{DFIGmin} are the maximum input power of the IDC and the minimum output power of the DFIG, respectively. For a given CSI-IDVR, its maximum compensation capacity should be designed, i.e., the voltage sag ratio and duration time available to be protected are determined. Therefore, the energy capacity of the SMES can be obtained.

To make the SMES current be within the required operating range, the two voltage reference signals, i.e., $u^-_{sd\mathrm{ref}-}$ and $u^-_{\mathrm{IDC}d\mathrm{ref}-}$, can be slightly adjusted within 0.95 pu ~ 1.05 pu. The block diagram of the SMES current control is shown in the Fig. 8.

5. Case study and simulation results

The renewable energy data center system integrated with SMES-based IDVR is modeled and analyzed in MATLAB/Simulink. Both the rated power of the IDC and the DFIG is 1.5 MW. In the two cases of 85% three-phase-to-ground (3LG) fault and 85% two-phase-to-ground (2LG) fault, the characteristics of DFIG and IDC with and without CSI-DVR protection are simulated and analyzed. Both faults occur at 0.2 s and are cleared at 0.8 s. To simplify the analysis, the DFIG wind speed is at the rated wind speed of 12 m/s. Simulation parameters of the DFIG, IDC, and SMES are shown in Tables 1-3 in the Appendix

5.1. Fault characteristic analysis of DFIG and IDC without protection

Assuming a 3LG fault with a depth of 85% occurs in the grid at *t*=0.2 s, and is relieved at 0.8 s. Without CSI-IDVR, the responses of grid-side voltage, active power, reactive power, and the DC, 60 Hz, and 120 Hz components of the active and reactive power are shown in Fig. 9. It can be seen from the Fig. 9(a) that at the fault occurrence and clearance, there will be high instantaneous power and huge oscillation in the output power of DFIG. During the whole transient process, the maximum active power and minimum active power of DFIG are 1.22 pu and -3.34 pu, respectively, and the maximum and minimum reactive power are 3.08 pu and -1.73 pu, respectively. The simulation results are consistent with the theoretical analysis in Section 3, i.e., the stator output power of the DFIG under symmetrical

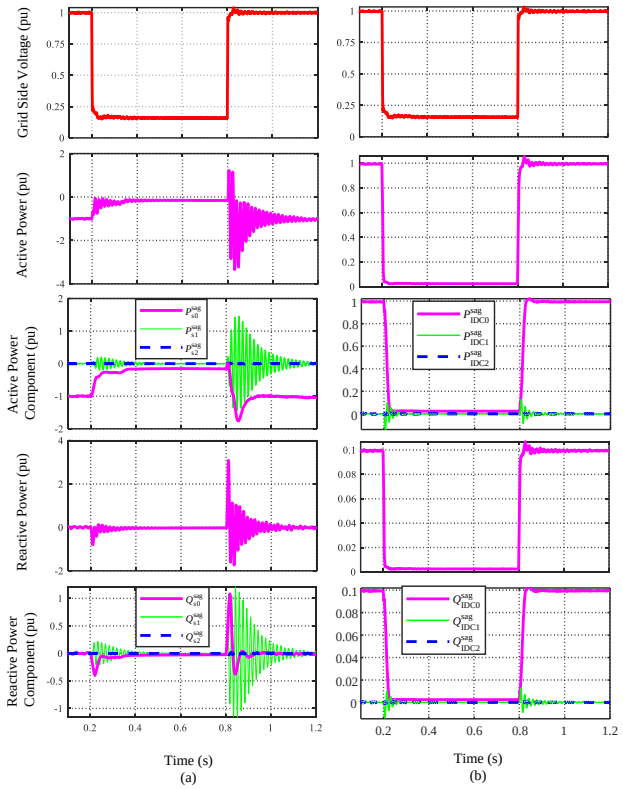

Fig. 9. Responses of the grid side voltage, active power, active power component, reactive power, and reactive power component of DFIG and IDC under 85% 3LG fault without protection. (a) DFIG side; (b) IDC side.

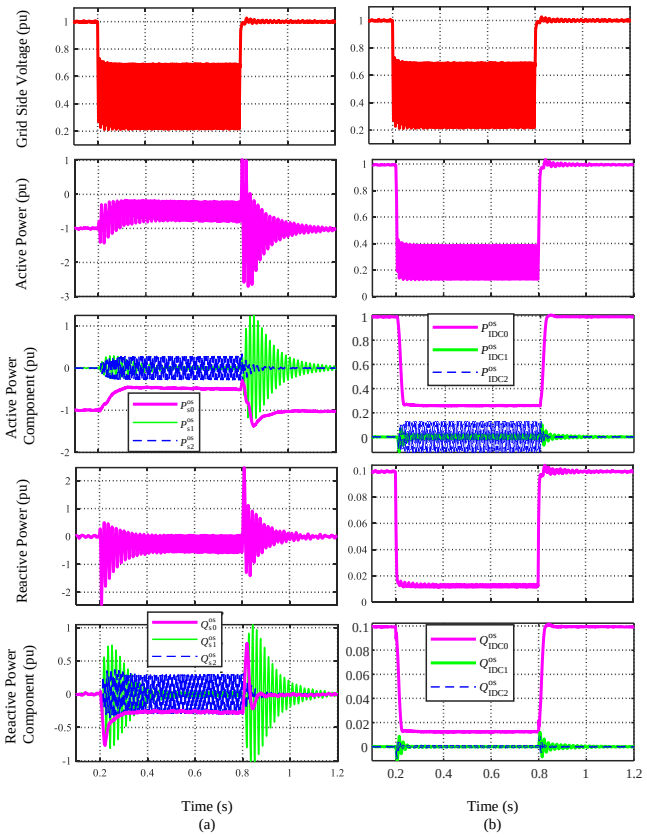

Fig. 10. Responses of the grid side voltage, active power, active power component, reactive power, and reactive power component of DFIG and IDC under 85% 2LG fault without protection. (a) DFIG side; (b) IDC side.

voltage fault includes the average active and reactive power P_{s0}^{sag} and Q_{s0}^{sag}, and the attenuating active and reactive power P_{s1}^{sag} and Q_{s1}^{sag} fluctuations with the frequency of ω_s. Compared with the Fig. 9(a), the power variation of the IDC can be seen in the Fig. 9(b), and the minimum active/reactive power of IDC is 0.023/0.002 pu. Since the DFIG and IDC are connected to the same 35 kV bus, the active and reactive power of the IDC also contain small 60 Hz oscillations, which can be seen in the Fig. 9(b) due to the slight influence of the DFIG. Overall, besides the change of the DC component, the standard deviations of P_{IDC1}^{sag} and Q_{IDC1}^{sag} are 0.017 and 0.0017, respectively, there is almost no fluctuation of the active and reactive power, and the power response of the IDC under symmetrical voltage sag is in line with (13).

Fig. 10 shows the parametric response of DFIG and IDC without protection under asymmetric fault. During the whole transient process, the maximum active power and minimum active power of DFIG are 1.02 pu and -2.70 pu, respectively, and the maximum and minimum reactive power are 2.47 pu and -2.44 pu, respectively. Different from the response under symmetrical fault, there are additional power fluctuation components (P_{s2}^{os} and Q_{s2}^{os}) with the frequency of $2\omega_s$ in the active and reactive power responses of the DFIG and IDC.

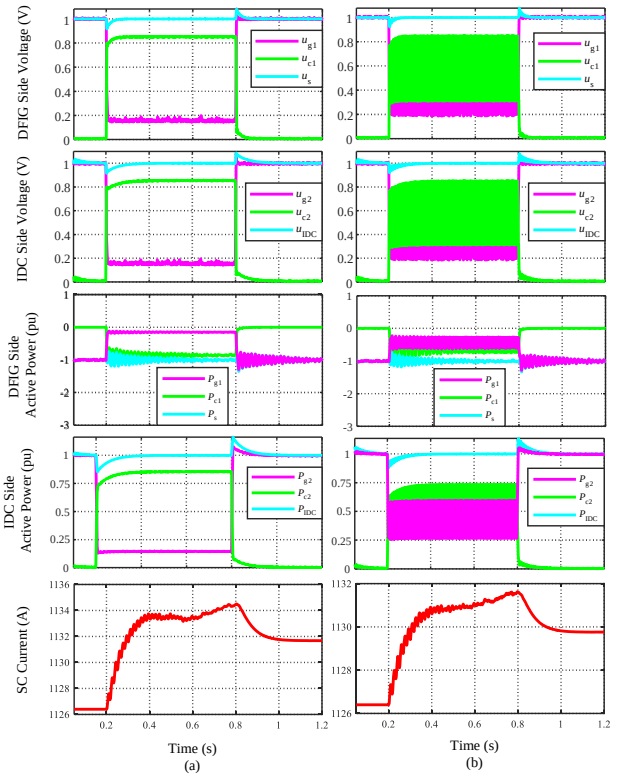

Fig. 11. Responses of the DFIG side voltage, IDC side voltage, DFIG side active power, IDC side active power, and the superconducting coil (SC) current. (a) under 85% 3LG fault with the proposed CSI-IDVR protection; (b) under 85% 2LG fault with the proposed CSI-IDVR protection.

5.2. Fault characteristic analysis of DFIG and IDC with proposed CSI-IDVR protection

With the protection of the proposed CSI-IDVR, the response of the voltage and active power of the DFIG and IDC and the SMES operating current under 85% 3LG and 2LG faults are shown in Figs. 11(a) and (b), respectively. The proposed CSI-IDVR can quickly inject the specific voltages u_{c1} and u_{c2} to maintain the terminal voltages of the DFIG and IDC (u_s and u_{IDC}) to the rated value when the fault occurs. After using the proposed CSI-IDVR protection, the peak-to-peak values of the u_s under 3LG fault and 2LG fault are within 0.16 pu and 0.15 pu, respectively, which means there are only small oscillations in the voltage curves at the fault occurrence and the fault clearance. The peak-to-peak values of the DFIG output power under 3LG fault and 2LG fault are limited to within 0.61 pu and 0.59 pu, respectively, which can be acceptable. Similarly, the peak-to-peak values of IDC side voltage under 3LG fault and 2LG fault are limited to within 0.17 pu and 0.16 pu, respectively, and the power of the IDC under symmetrical faults or asymmetrical faults is well-maintained at 1.0 pu.

As analyzed in Section 2, in this simulation, the absorbed and released power of the SMES almost reaches equilibrium since the power of the DFIG and IDC are at the rated value. Due to the existence of P_{s1}, there will be a slight difference in SC current before and

after the fault, but the overall change is very small. It can be seen from the Fig. 11 that before and after the symmetrical and asymmetrical faults, the operating current of the SMES is increased from 1126.3 A to 1134.4 A and 1131.7 A, respectively. Calculating the energy change between the occurrence (0.2 s) and the end (0.8 s) of the fault, the energy absorption of the SMES ~ 11.77 kJ and ~ 7.83 kJ, respectively.

In the cases without protection and with the proposed CSI-IDVR protection, the responses of the DFIG's crucial parameters including the Electromagnetic torque (T_{em}), the amplitude of the rotor current (I_{ramp}) and the angular frequency of DFIG rotor (ω_{r}) under 3LG and 2LG faults are shown in Fig. 12. In the figure label, subscripts 0 and 1 indicate unprotected and protected status, respectively. It can be found that under 85% 3LG faults, with the proposed CSI-IDVR protection, the peak-to-peak values of T_{em}, I_{ramp} and ω_{r} can be limited from 4.55 pu, 4.24 pu, and 0.089 pu to 0.62 pu, 0.51 pu, and 0.004 pu. Similarly, under 85% 2LG faults, the peak-to-peak values of T_{em}, I_{ramp} and ω_r can be limited from 4.43 pu, 4.31 pu, and 0.048 pu to 0.65 pu, 0.52 pu, and 0.003 pu with the assistance of the proposed method. Accordingly, the proposed CSI-IDVR protection can effectively suppress the oscillation of the above DFIG's crucial parameters under both symmetric and asymmetric faults.

5.3. Energy variation of the SMES in CSI-IDVR

To estimate the energy-saving proportion of the CSI-IDVR compared to separate DVR, three different wind speed conditions of the DFIG are considered, where the output power of the DFIG is 0.6 pu (low wind speed), 1.0 pu (rated wind speed), and 1.4 pu (high wind speed), respectively. Under the simulated 3LG fault, the energy variations of the SMES in the proposed CSI-IDVR protection scheme and two independent DVRs protection scheme are shown in Fig. 13.

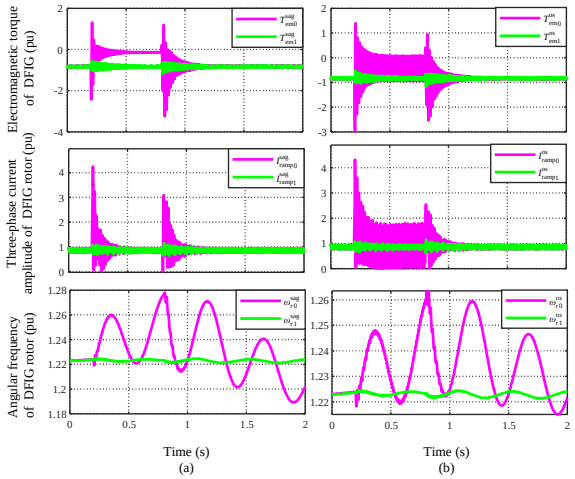

Fig. 12. Responses of the DFIG's electromagnetic torque, the amplitude of the rotor current, and the angular frequency of the DFIG rotor without protection and with the proposed CSI-IDVR protection. (a) under 85% 3LG fault; (b) under 85% 2LG fault.

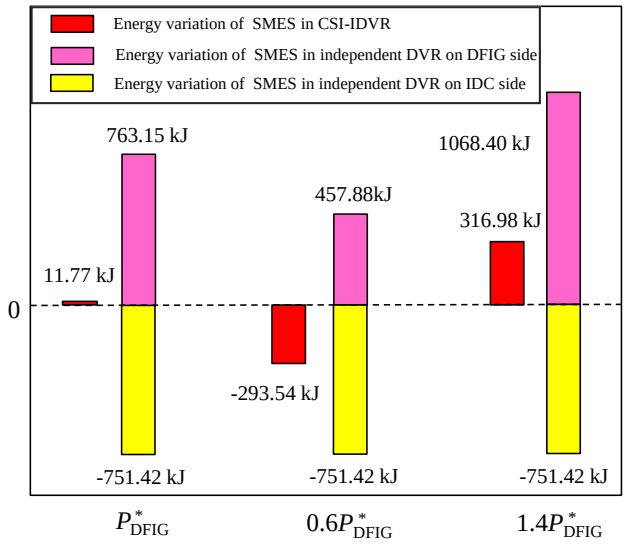

Fig. 13. Energy variation of SMES in the proposed CSI-IDVR protection scheme and in two independent DVRs protection scheme during 3LG grid fault.

It can be seen from the Fig. 13 that in two independent DVRs, the energy variations of the SMES on the IDC side are all -751.42 kJ, while the energy absorbed by the SMES on the DFIG side is affected by the wind speed. Under three power conditions (0.6 pu, 1.0 pu, and 1.4 pu), the energy absorption of the DFIG-side DVR is 457.88 kJ, 763.15 kJ, and 1068.40 kJ, respectively. To deal with the transient energy of the IDC and DFIG, the required energy in the SMES (E^*_{SMES}) are 1209.3 kJ, 1514.57 kJ, and 1819.82 kJ capacity in total in the scheme with two individual DVRs. In the proposed CSI-IDVR protection scheme, part of the energy absorbed from the DFIG is then released to the IDC The required energy of the SMES during three conditions are only -293.54 kJ, 11.77 kJ, and 316.98 kJ, respectively, only 24.27%, 0.78%, and 17.42% of the individual-DVR scheme.

5.4. Comparison of CSI- and VSI-based DVR

CSI-based DVR is an emerging device, and the technology is gradually investigated recently. Therefore, it is necessary to conclude the characteristics of the CSI when used as the converter of the DVR. The advantages and drawbacks by comparing the CSI- and VSI-based DVR are shown as follows:

Advantages:

i) CSI has inherent four-quadrant operation capability and does not require an additional converter on the DC bus. Therefore, it fits the characteristics of the current-type energy storage especially SMES, simplifying the structure configuration. On the other hand, VSI requires a regenerative converter on the DC link.

ii) CSI is more robust and does not exist problems such as shoot-through faults. Momentary short-circuits in the load and the misfiring of thyristors can be withstood [51].

iii) In addition to ii), CSI is more reliable in large-power

applications, such as large-power offshore wind farms. Some references have discussed this characteristic of current-fed back-to-back converters [52, 53].

iv) Due to the existence of the inductor, a CSI-based DVR can efficiently constrain the change rate of a fault current during voltage abruption while enhancing the load voltage to the rated profile. The function of the inductor can be referred to [54], which analysis the inductive-type (SMES) superconducting fault current limiter from the perspective of circuit modeling. In this paper, A controllable SMES-based DVR has been carried out in this work with emphasis of its dynamic voltage control.

Drawbacks:

i) Devices must be symmetric blocking in a CSI system, unlike the asymmetric blocking devices (with bypass diode) in a VSI. This characteristic of CSI means that the power electronic switches with higher voltage tolerance are required.

ii) In addition to i), from the perspective of overall efficiency, a VSI system is superior.

iii) The operation of a CSI requires a minimum load that always remains connected. The inability to operate at no-load conditions confines its application in many areas. Merely, CSI-based DVR does not exist this issue due to its serial connection configuration, since the transmission line current will not be zero.

iv) CSI cannot be operated in an open-loop mode, whereas open-loop control of a VSI (such as open-loop *v*/*f* control) is relatively common.

6. Conclusion

This paper proposes a new CSI-IDVR based on SMES to protect sensitive generators and loads simultaneously in a data center power system with renewable energy power supply and provides systematical designs of topological structure and cooperative control strategy of the proposed scheme.

The simulation results show that under 85% 3LG and 2LG faults, the proposed protection scheme can quickly compensate the required voltage and keep both DFIG and IDC side voltages at around 1.0 pu and limit their peak-to-peak values at around 0.16 pu. The voltage fluctuation and power oscillation of DFIG and IDC can be effectively suppressed. In the proposed scheme, the SMES can absorb part of the DFIG-generated energy, meanwhile compensating the lacking energy of IDC. Compared with the individual-DVR protection scheme, the capacity requirement of the SMES is largely reduced, greatly saving the cost of the SMES and efficiently coordinating the energy conversion among DFIG, SMES, and IDC. The proposed protection scheme can be commonly applied to sensitive generators/loads composited systems. It is expected to provide a new solution to utilize renewable energy under transient conditions and reduce the required energy storage capacity.

Appendix

TABLE 1
PARAMETERS OF DFIG

Parameter	Value
Rated power	1.5 MW
Rated rotor voltage	1725 V
Rated stator voltage	690 V
Rated wind speed	12 m/s
Rotor resistance	0.005 pu
Stator resistance	0.007 pu
Rotor leakage inductance	0.156 pu
Stator leakage inductance	0.171 pu
Mutual inductance	2.9 pu
DC-link capacitor	10 mF
Rated DC-link voltage	1200 V

TABLE 2
PARAMETERS OF IDC

Parameter	Value
Rated voltage	1 kV
Rated power of the computing load	150 W
Rated power of the PSU	1.5 kW
Number of the server rack in a server room	300
Number of the PDUs	3
Rated power of the cooling system	100 kW
Rated power of the lighting system	50 kW
Number of racks	3
Rated IDC System power	1.5 MW

TABLE 3
PARAMETERS OF IDVR

Parameter	Value
DFIG side transformer ratio	690 V/1380 V
IDC side transformer ratio	1 kV/ 2 kV
Capacitance of the CL filter	3000 μF
Inductance of the CL filter	10 μH
SC inductance	1.285 H
SC initial operating current	1126.3 A
SC critical current	1321 A
Energy capacity of the SMES	1.12 MJ

REFERENCES

[1] J. Sun, S. Wang, J. Wang, L. M. Tolbert, Dynamic model and converter-based emulator of a data center power distribution System, IEEE Trans. Power Electron. 37 (7) (2022) 8420-8432..

[2] Power quality in internet data centers, Electr. Power Res. Inst., Palo Altok, CA, USA (2007).

[3] T. Yang, Y. Zhao, H. Pen, Z. Wang, Data center holistic demand response algorithm to smooth microgrid tie-line power fluctuation, Appli. Energy, 231 (2018) 277-287.

[4] R. Rahmani, I. Moser, A. L. Cricenti, Modelling and optimisation of microgrid configuration for green data centres: A metaheuristic approach, Future Gener. Computer Syst., 108 (2020) 742-750.

[5] L. Liu, H. Sun, C. Li, T. Li, J. Xin, N. Zheng, Managing battery aging for high energy availability in green datacenters, IEEE Trans. Parallel Distri. Syst. 28 (12) (2017) 3521-3536.

[6] Z. Chai, H. Li, X. Xie, M. Abdeen, T. Yang, K. Wang, Output impedance modeling and grid-connected stability study of virtual synchronous control-based doubly-fed induction generator wind turbines in weak grids, Int. J. Electr. Power Energy Syst. 126 (A) (2021) 106601.

[7] S. A. A. Shahriari, M. Mohammadi, M. Raoofat, A new method based on state-estimation technique to enhance low-voltage ride-through capability of doubly-fed induction generator wind turbines, Int. J. Electr. Power Energy Syst. 95 (2018) 118-127.

[8] M. Farhadi-Kangarlu, E. Babaei, F. Blaabjerg, A comprehensive review of dynamic voltage restorers, Int. J. Electr. Power Energy Syst. 92 (2017) 136-155.

[9] B. R. Shrestha, U. Tamrakar, T. M. Hansen, B. P. Bhattarai, S. James, R. Tonkoski, Efficiency and reliability analyses of AC and 380 V DC distribution in data centers, IEEE Access. 6 (2018) 63305-63315.

[10] J. He, X. Xiao, R. Zhong, W. Huang, D. Li, Q. Chen, New AC & DC hybrid power supply system and its reliability analysis in data centre, J. Engineering, 16 (2019) 2800-2803.

[11] G. A. Parameswari, H. H. Sait, A comprehensive review of fault ride-through capability of wind turbines with grid-connected doubly fed induction generator, Int. Trans. Electr. Energy Syst. 30 (8) (2020) e12395.

[12] Z. Din, J. Zhang, Z. Xu, Y. Zhang, J. Zhao, Low voltage and high voltage ride-through technologies for doubly fed induction generator system: Comprehensive review and future trends, IET Renew. Power Gener. 15 (3) (2021) 614-630.

[13] T. Addabbo, A. Fort, M. Mugnaini, V. Vignoli, E. Simoni, M. Mancini, Availability and reliability modeling of multicore controlled UPS for datacenter applications, Reliab. Eng. Syst. Saf. 149 (2016) 56-62.

[14] J. Sun, M. Mihret, M. Cespedes, D. Wong and M. Kauffman, Data center power system stability — Part II: System modeling and analysis, CSEE J. Power Energy Syst. 8 (2) (2022) 420-438.

[15] R. S. Camargo, A. E. A. Amorim, E. J. Bueno, L. F. Encarnação, Novel multilevel STATCOM for power system stability enhancement on DFIG-based wind farms, Electric Power Syst. Res. 197 (2021) 107316.

[16] R. H. Yang, J. X. Jin, Unified Power Quality Conditioner with Advanced Dual Control for Performance Improvement of DFIG-Based Wind Farm, IEEE Trans. Sust. Energy. 12 (1) (2021) 116-126.

[17] J. X. Jin, R. H. Yang, R. T. Zhang, Y. J. Fan, Q. Xie, X. Y. Chen, Combined low voltage ride through and power smoothing control for DFIG/PMSG hybrid wind energy conversion system employing a SMES-based AC-DC unified power quality conditioner, Int. J. Electr. Power Energy Syst. 128 (2021) 106733.

[18] M. D. B. Gomes; M. C. Cavalcanti; L. R. Limongi; G. M. S. Azevedo, M. E. C. Brito, A twelve-switch power conditioner for voltage and current compensation in three-phase four-wire grids, Int. J. Electr. Power Energy Syst. 138 (2022) 107881.

[19] C. Wessels, F. Gebhardt, F. W. Fuchs, Fault Ride-Through of a DFIG wind turbine using a dynamic voltage restorer during symmetrical and asymmetrical grid faults, IEEE Trans. Power Electron. 26 (3) (2011) 807-815.

[20] R. Nasrollahi, H. Feshki Farahani, M. Asadi, M. Farhadi-Kangarlu, Sliding mode control of a dynamic voltage restorer based on PWM AC chopper in three-phase three-wire systems, Int. J. Electr. Power Energy Syst. 134 (2022) 107480.

[21] A. H. Soomro, A. S. Larik, M. A. Mahar, A. A. Sahito, A. M. Soomro, G. S. Kaloi, Dynamic voltage restorer—A comprehensive review, Energy Reports, 7 (2021) 6786-6805.

[22] M. Moradlou, H. R. Karshenas, Design strategy for optimum rating selection of interline DVR, IEEE Trans. Power Deli. 26 (1) (2011) 242-249.

[23] Y. Mishra, S. Mishra, F. Li, Coordinated Tuning of DFIG-Based Wind Turbines and Batteries Using Bacteria Foraging Technique for Maintaining Constant Grid Power Output, IEEE Syst. J. 6 (1) (2012) 16-26.

[24] T. Mesbahi, A. Ouari, T. Ghennam, E. M. Berkouk, N. Rizoug, N. Mesbahi, M. Meradji, A stand-alone wind power supply with a Li-ion battery energy storage system, Renew. Sust. Energy Reviews 40 (2014) 204-213.

[25] M. K. Döşoğlu, A. B. Arsoy, Transient modeling and analysis of a DFIG based wind farm with supercapacitor energy storage, Int. J. Electr. Power Energy Syst 78 (2016) 414-421.

[26] M. K. Döşoğlu, O. Özkaraca, U. Güvenç, Novel active–passive compensator–supercapacitor modeling for low-voltage ride-through capability in DFIG-based wind turbines, Electr Eng 101 (2019) 1119–1132.

[27] S. Mukoyama et al., Development of Superconducting Magnetic Bearing for 300 kW Flywheel Energy Storage System, IEEE Trans. Appli. Supercond 27 (4) (2017) 3600804.

[28] H. Ihssen, B. Farid, T. Abdelaziz, Advanced control for wind energy conversion systems with flywheel storage dedicated to improving the quality of energy," Int. J. Hydrogen Energy 41 (45) (2016) 20832-20846.

[29] D. Vilathgamuwa, H. M. Wijekoon, S. S. Choi, A Novel technique to compensate voltage sags in multiline distribution system—The interline dynamic voltage restorer, IEEE Trans. Ind. Electron. 53 (5) (2006) 1603-1611.

[30] L. Gyugyi, K. K. Sen, C. D. Schauder, The interline power flow controller concept: a new approach to power flow management in transmission systems, IEEE Trans. Power Deli. 14 (3) (1999) 1115-1123.

[31] A. Elserougi, A. M. Massoud, A. S. Abdel-Khalik, S. Ahmed, A. A. Hossam-Eldin, An interline dynamic voltage restoring and displacement factor controlling device (IVDFC), IEEE Trans. Power Electron. 29 (6) (2014) 2737-2749.

[32] R. P. Usha, R. Sudha, S. R. Reddy, Voltage sag/swell compensation in an interline dynamic voltage restorer, 2011 International Conference on Emerging Trends in Electrical and Computer Technology, 2011, 309-314.

[33] L. Zhang, P. C. Loh, F. Gao, B. Frede, Reduced semiconductor three-level interline dynamic voltage restorer, 8th International Conference on Power Electronics - ECCE Asia, 2011, 1843-1847.

[34] M. Shahabadini, H. Iman-Eini, Improving the performance of a cascaded H-bridge-based interline dynamic voltage restorer, IEEE Trans. Power Deli. 31 (3) (2016) 1160-1167.

[35] X. Chen, Q. Xie, X. Bian, B. Shen, Energy-saving superconducting magnetic energy storage (SMES) based interline DC dynamic voltage restorer, CSEE J. Power Energy Syst. 8 (1) (2022) 238-248.

[36] S. I. Gkavanoudis, C. S. Demoulias, Fault ride-through capability of a DFIG in isolated grids employing DVR and supercapacitor energy storage, Int. J. Electr. Power Energy Syst. 68 (2015) 356-363.

[37] S. Hasan, K. M. Muttaqi, D. Sutanto, M. A. Rahman, A novel dual slope delta modulation technique for a current source inverter based dynamic voltage restorer for mitigation of voltage sags, IEEE Trans. Ind. Appli. 57 (5) (2021) 5437-5447.

[38] S. A. Verne, M. I. Valla, Dynamic voltage restorer based on multilevel current source inverters, 2018 Argentine Conference on Automatic Control (AADECA), 2018, 1-6.

[39] J. Ren, X. Xiao, Z. Zheng, Application of CSC-based SMES to improve the LVRT capability of DFIG-based WECS, 2020 IEEE International Conference on Applied Superconductivity and Electromagnetic Devices (ASEMD), 2020, 1-2.

[40] J. Ren, X. Xiao, Z. Zheng, Z. Ma, A SMES-based dynamic current limiter to improve the LVRT capability of DFIG-based WECS, IEEE Trans. Appli. Supercond. 31 (8) (2021) 5401805.

[41] E. P. Wiechmann, P. Aqueveque, R. Burgos, J. Rodriguez, On the efficiency of voltage source and current source inverters for high-power drives, IEEE Trans. Ind. Electron. 55 (4) (2008) 1771-1782.

[42] M. Elshiekh, A. Elwakeel, S. Venuturumilli, H. Alafnan, X. Pei, M. Zhang, W. Yuan, Utilising SMES-FCL to improve the transient behaviour of a doubly fed induction generator DC wind system, Int. J. Electr. Power Energy Syst. 131 (2021) 107099.

[43] T. Karaipoom, I. Ngamroo, Optimal superconducting coil integrated into DFIG wind turbine for fault ride through capability enhancement and output power fluctuation suppression, IEEE Trans. Sust. Energy, 6 (1) (2015) 28-42.

[44] F. Alskran, M. G. Simões, Multilevel current source converter-based STATCOM suitable for medium-voltage applications, IEEE Trans. Power Deli. 36 (2) (2021) 1222-1232.

[45] Ali Q. Al-Shetwi, M. A. Hannan, K. P. Jern, M. Mansur, T. M. I. Mahlia, Grid-connected renewable energy sources: Review of the recent integration requirements and control methods, J. Clean. Produc. 253 (2020) 119831.

[46] IEEE recommended practice for powering and grounding electronic equipment, IEEE Std 1100-2005 (Revision of IEEE Std 1100-1999), (2006) 1-703.

[47] M. Y. Zargar, M. U.-D. Mufti, S. A. Lone, Adaptive predictive control of a small capacity SMES unit for improved frequency control of a wind-diesel power system, IET Renew. Power Gener. 11 (14) (2017) 1832-1840.

[48] J. Lopez, P. Sanchis, X. Roboam, L. Marroyo, Dynamic behavior of the doubly fed induction generator during three-phase voltage dips, IEEE Trans. Energy Conv. 22 (3) (2006) 709-717.

[49] G. Abad, J. Lopez, M. Rodriguez, L. Marroyo, G. Iwanski, Doubly fed induction machine: modeling and control for wind energy generation IEEE Wiley, Hoboken, NJ, USA (2011).
[50] Y. Ye, M. Kazerani V. H. Quintana, Modeling, control and implementation of three-phase PWM converters, IEEE Trans. Power Electron. 18 (3) (2003) 857-864.
[51] B. K. Bose, Modern power electronics and AC drives, Prentice Hall PTR, Upper Saddle River, NJ, USA (2001).
[52] Z. Wang, B. Yuwen, Y. Lang, M. Cheng, Improvement of Operating Performance for the Wind Farm With a Novel CSC-Type Wind Turbine-SMES Hybrid System, *IEEE Trans. Power Delivery*, 28 (2) (2013) 693-703.
[53] R. E. Torres-Olguin, A. Garces, M. Molinas and T. Undeland, Integration of Offshore Wind Farm Using a Hybrid HVDC Transmission Composed by the PWM Current-Source Converter and Line-Commutated Converter, IEEE Transactions on Energy Conversion, 28 (1) (2013) 125-134.
[54] W. Guo, L. Xiao and S. Dai, Enhancing Low-Voltage Ride-through capability and smoothing output power of DFIG with a superconducting fault-current limiter-magnetic energy storage system, IEEE Trans. on Energy Conversion, 27 (2) (2012) 277-295.